Materials Today 95 (2026) 103280

Contents lists available at ScienceDirect

Materials Today

journal homepage: www.elsevier.com/locate/mattod

Ultrafine CoCrCuFeNi high entropy alloy thin films with high strength, plastic deformability and thermal stability achieved via grain engineering and nanoclustering

Davide Vacirca [a,*], Francesco Bignoli [a,b], Andrea Li Bassi [b], Yuting Dai [c,f], Ali Ahmadian [c,f], Gregory Abadias [d], Philippe Djemia [a], Gerhard Dehm [e], James P. Best [e], Matteo Ghidelli [a,*]

[a] Laboratoire des Sciences des Procédés et des Matériaux (LSPM)-CNRS, UPR 3407, Université Sorbonne Paris Nord, 93430 Villetaneuse, France
[b] Dipartimento di Energia, Laboratorio Materiali Micro e Nanostrutturati, Politecnico di Milano I-20133 Milano, Italy
[c] Institute of Nanotechnology, Karlsruhe Institute of Technology, Eggenstein-Leopoldshafen, Germany
[d] Institut Pprime, UPR 3346, CNRS-Université de Poitiers-ENSMA, 86073 Poitiers Cedex 9, France
[e] Max Planck Institute for Sustainable Materials, 40237 Düsseldorf, Germany
[f] Karlsruhe Nano-/Micro Facility (KNMFi), Karlsruhe Institute of Technology, Eggenstein- Leopoldshafen, Germany

ARTICLE INFO

Keywords:
High entropy alloy thin films
Mechanical properties
Thermal stability
Grain engineering
Pulsed laser deposition

ABSTRACT

The design of high-performance structural materials is always pursuing the combination of mutually exclusive properties such as mechanical strength, plasticity and thermal stability. Although high entropy alloys thin films (HEAs-TF) show promising mechanical and thermal properties, the development of novel nanostructures with unique nanoscale features is needed to overcome the strength-plasticity-thermal stability trade-off, going beyond a conventional compositional control. Here, we present a new synthesis route to fabricate ultra-strong, highly plastic, and thermally stable HEAs-TF leveraging the unique capabilities of pulsed laser deposition (PLD). We demonstrate our approach by focusing on CoCrCuFeNi, a model FCC HEA of the original Cantor family. Specifically, we synthetize ultrafine grain structures with controllable size (down to 12 nm) which can be further tailored by post-thermal annealing treatments, resulting in high hardness (11 GPa) and yield strength (2.0 GPa) due to Hall-Petch strengthening, outperforming similar HEAs-TF while maintaining high plasticity (no fracture at 30% strain). Moreover, these ultrafine HEAs-TF shows enhanced thermal stability, grain growth starting at $T = 49\%$ of T_m (melting temperature), while maintaining high hardness (9.1 GPa) after annealing for 1 h at 460°C. The PLD-deposited ultrafine HEAs-TF lead to mutual thermodynamic and mechanical stabilization, opening up a new approach for stable, strong and ductile materials.

Introduction

Grain refinement in metallic materials is a well-known route to increase yield strength, hindering the movement of dislocations at the grain boundaries, triggering Hall-Petch strengthening [1,2]. Such phenomenon is observed for nanocrystalline (nc) metals with average grain size down to ~10 nm. However, Hall-Petch strengthening is often accompanied by a lower thermal stability, especially for nc metals, due to the high density of grain boundaries promoting atomic interdiffusion and rapid grain growth [3]. In addition, an inverse Hall-Petch regime is triggered for grain sizes <10 nm, in which plastic deformation is facilitated at lower stresses by grain rotation or sliding [4]. Moreover, plastic deformability is also known to worsen as the grain size decreases to the nanometer scale due to lowered intragranular dislocation activity [5]. For these reasons, achieving a mutual combination of high yield strength, thermal stability and ductility is challenging, usually requiring an appropriate chemical design approach, resulting in solid solution strengthening and thermal stability, together with the control of the grain size through a grain engineering approach.

In this regard, high entropy alloys (HEAs) also known as compositionally complex alloys (CCAs), have recently gained interest due to their better thermal and mechanical properties [6,7], such as high thermal stability compared to traditional alloys [8], together with high yield strength and plastic deformability [9]. HEAs are multicomponent metallic materials constituted of at least 4 different elements with an equiatomic (or near equiatomic) composition, as opposed to

* Corresponding authors.
E-mail addresses: davide.vacirca@lspm.cnrs.fr (D. Vacirca), matteo.ghidelli@lspm.cnrs.fr (M. Ghidelli).

https://doi.org/10.1016/j.mattod.2026.103280
Received 14 May 2025; Received in revised form 27 January 2026; Accepted 3 March 2026
Available online 11 March 2026

conventional alloys that primarily consist of one principal element with solute atoms addition [10]. In their original description, Cantor [11] and Ye [10] defined some of the key structural features of HEAs such as their high mixing entropy or lattice distortion [12,13], in order to explain their phase stability as well as the mechanical and thermal behavior. For instance, the strong lattice distortion originates from the mismatch in atomic radii among the HEA's constituents, and has been directly linked to an increase in yield strength as a result of solid solution strengthening (from 200 to 800 MPa for $Al_xCoCrFeMnNi$) [14], in which dislocation motion is impeded by the presence of larger atoms, as shown by Varvenne *et al.* [15] for FCC HEAs. Furthermore, different studies have highlighted the thermal stability of bulk HEAs, which can be explained by the sluggish diffusion. For this reason, some HEA have been proposed as valid alternatives to Ni-based superalloys [16].

Bulk HEAs synthetized with traditional methods (including arc melting, casting, hot isostatic pressing) can only achieve a grain size in the micrometer range, while nanometer scale grain refinement is difficult to obtain due to the slow cooling rate. For instance, L. Brocq *et al.* [17], fabricated 12 μm grain size CoCrFeMnNi with low hardness (~3 GPa) and yield strength (~320 MPa) resulting from limited Hall-Petch strengthening. Nanometer grain sizes (down to ~ 50 nm) can be fabricated by high-pressure torsion (HPT) [18] in which severe plastic deformation is exploited to induce a strong grain refinement. Alternatively, other techniques such as mechanical alloying or spark plasma sintering can induce small grain sizes of few tens of nanometers for HEAs due to the faster cooling rates [19]. Finally, recent studies have shown that implementing rare earth elements into the design of HEAs can stabilize the grain boundaries, enabling to easily produce bulk nanocrystalline HEAs while enhancing thermal stability, as reported for $(CoCrFeNi)_{96}Sm_4$ [20]. However, both techniques have limitations involving a dual step synthesis and/or the difficulty to control complex chemical composition, which often result in inhomogeneous structures with segregation or secondary phases [21].

HEAs in their thin film form (HEAs-TF) have only recently attracted significant interest [22], with potential applications as structural coatings, improving the mechanical and thermal performance of the underlying substrate [23], as well as in microelectronics, energy systems and a variety of industrial technonologies [24]. HEAs-TF usually possess nanosized grains due to thickness confinement and fast cooling rates, leading to Hall-Petch strengthening, further enhancing mechanical properties. For example, Zou *et al.* [25] fabricated nc refractory NbMoTaW films with grain size <100 nm and BCC phase, showing high yield strength (up to 6.5 GPa) which is kept at high temperature (600°C), which however possesses limited plasticity. Another advantage of TFs is represented by the possibility to easily synthesize complex nanostructures that can be exploited to further boost their mechanical properties and thermal stability. For instance, Wu *et al.* [26] synthetized HEAs-TF nanolaminates with FCC/amorphous phases, reaching hardness up to 11 GPa after annealing at 700°C for 1 h, and homogeneous plastic deformation up to 15% of compressive strain.

In this context, one of the main challenges in HEAs-TF is represented by the development of novel materials with unique and tailored microstructural and compositional features capable to trigger Hall-Petch strengthening, while keeping large plastic deformability and thermal stability capable to meet specific industry requirements and develop materials resistant to intense thermo-mechanical solicitations. This is especially crucial for FCC-based HEAs which usually have low yield strength but high ductility [27], and more complex deposition steps, i.e. fabrication of multiphase (FCC/BCC, FCC/amorphous [26]) nanolaminates are needed to improve their strength and thermal stability.

Magnetron sputtering is by far the most used technique for the synthesis of HEAs-TF, due to the potential industrial scalability. However, a major limitation of this technique is represented by the restricted control of TF microstructural features, since it is intrinsically dependent on the plasma conditions, which can only be sustained over a narrow pressure range [28]. This limits the film's nanoengineering possibilities, making it impossible to achieve complex architectures such as cluster-assembled microstructures. Alternative techniques for HEA-TF synthesis are rarely explored in literature. For example, electrodeposition has been proposed, but it lacks precise control over chemical composition – a critical requirement for complex alloys such as HEAs – and typically results in films with rough surfaces and structural defects such as cracks [29].

In this regard, pulsed laser deposition (PLD) is known for being an extremely out-of-equilibrium deposition method [30], and can overcome the limitation of sputter-deposition by directly providing control over the energy of the deposited species depending on external and controllable parameters such as laser fluence, wavelength as well as the deposition pressure [31], which can lead to the synthesis of novel nanostructured metallic TFs. Depositions performed under vacuum conditions at low pressures (i.e. $\sim 10^{-3}$ Pa) lead to a high kinetic energy of the ablated species, which retain a larger mean free path due to minimal collision probability along the target–substrate trajectory [31]. Upon reaching the substrate, these energetic species exhibit high surface mobility, promoting an atom-by-atom growth regime, with a resulting film typically characterized by high density and a compact morphology with relatively large grains [32]. In contrast, introducing an inert background gas at higher pressures ($P > 1$ Pa) confines the plasma plume, facilitating the in-plume nanocluster nucleation. These nanoclusters, owing to their larger cross-section and the increased collision frequency at higher background gas pressure, exhibit a significantly reduced mean free path. Consequently, they land at the substrate with lower energy and mobility, leading to a cluster-assembled growth regime of the film characterized by nanogranular microstructure with smaller grains/domains [33]. For this reason, such morphologies have been defined as "compact" and "nanogranular", respectively for atom-by-atom and cluster assembled growth [34].

In our pioneer studies [34,35], we have shown how PLD can be used for the nanoengineering of TF metallic glasses with compact and nanogranular features or fabricating ultrafine nanolaminates, leading to a controllable and unique mechanical behavior. Specifically, we have shown that ultrafine structures obtained by nanoclustering can improve the ductility up to 9% for ZrCu TF metallic glasses, while blocking the propagation of shear bands [34].

Few literature studies deal with HEAs synthetized by PLD, mostly focusing on standard characterization [36] or studying the effect of chemical composition [37]. However, a grain engineering approach has never been applied for HEAs-TF, boosting the potential of PLD to create new phases and novel microstructures specifically designed to overcome the strength-plasticity-thermal stability trade-off, while providing a multiscale characterization from the micro down to the nanoscale.

Here, we push the boundaries of PLD to develop a novel class of HEAs-TF with ultrafine and tailored grain size (from 38 down to 12 nm) by simply controlling the deposition pressure during deposition, observing a transition from atom-by-atom growth to cluster assembled growth. Moreover, we demonstrate our approach by synthetizing a model FCC CoCrCuFeNi HEA, one of the first HEAs produced by Cantor [21], with nanocrystalline features resulting in a mutual combination of ultrahigh hardness and yield strength (respectively, ~11 and 2.0 GPa) compared to coarse-grained sputter deposited films (8.3 GPa), while maintaining high plastic deformability (>30%). In addition, post-thermal annealing treatments highlight the superior thermal stability of nanogranular PLD-deposited HEAs-TF compared to traditional alloys, showing higher thermal stability with grain growth being delayed until 400°C.

Results

Structural characterization of CoCrCuFeNi HEAs-TF

Fig. 1 a-c shows the SEM cross section of different CoCrCuFeNi HEAs-TF synthetized by PLD and magnetron sputtering. Films deposited by PLD at 2×10^{-3} Pa (Fig. 1a) are compact and nanocrystalline as a result

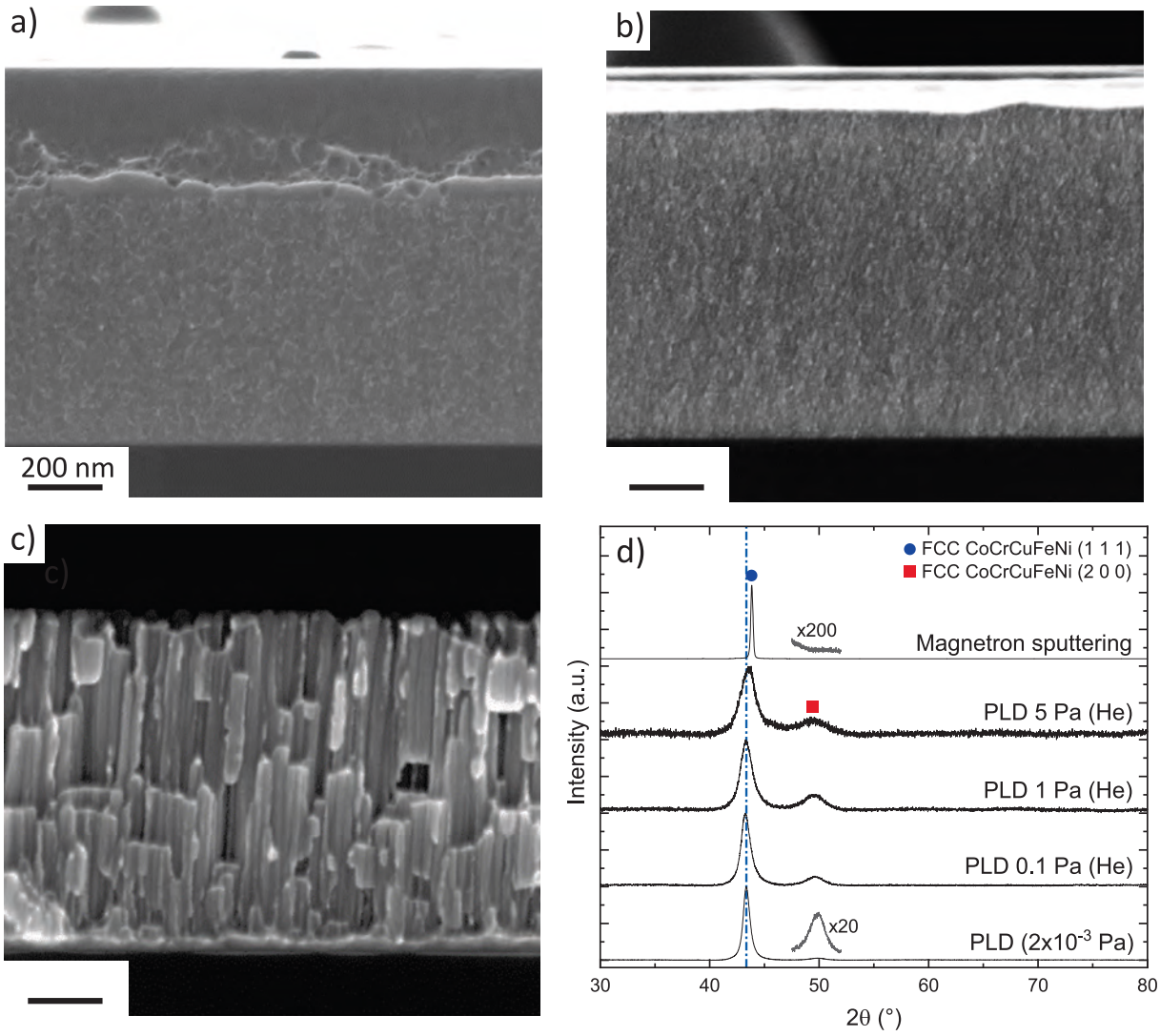

Fig. 1. SEM cross-sectional micrographs of CoCrCuFeNi HEAs-TF synthetized with different deposition techniques and conditions: a, b) PLD, respectively, 2×10^{-3} Pa and 5 Pa He, c) Magnetron sputtering. While PLD-deposited HEAs-TF are nanocrystalline with some nanogranular features for samples deposited at 5 Pa, the sputtering counterpart shows coarse columnar grains along the growth direction. The scale bar is equal for all micrographs. d) The corresponding normalized XRD diffractograms, showing a single FCC phase for all samples and different FWHM for the (1 1 1) peak increasing at higher deposition pressures. The magnified regions around 50° confirms the absence of the (2 0 0) reflection for the sputter-deposited film, indicating a strong (1 1 1) texture. A vertical dotted line following the (1 1 1) peak was added as a visual guide highlighting the shift in the peak position, resulting from the different deposition methods.

of the high energy of the ablated species [31]. At higher background gas pressures, the plasma confinement and the lower energy induces a cluster assembled growth [34], leading to the nanogranular morphology as shown in Fig. 1b. The difference between compact and nanogranular morphologies is better highlighted by TEM characterization (Fig. 2). On the other hand, HEAs-TF by magnetron sputtering show coarse columnar grains with an average diameter of 42 ± 6 nm. This is a typical morphology obtained by magnetron sputtering when depositing with similar deposition parameters at room temperature, as reported in other studies dealing with HEAs-TF [38].

XRD measurements in Fig. 1d reveal that all HEAs-TF have peaks matching with the FCC phase observed in previous works on CoCrCuFeNi [39], and further confirmed by TEM analyses (Fig. 2). Moreover, the lattice parameters equal to 3.60 and 3.58 Å for the PLD and sputter-deposited HEAs-TF respectively, are in agreement with literature results for bulk CoCrCuFeNi (3.61 Å) [39]. The FWHM of the (1 1 1) peak of HEAs-TF by PLD increases monotonically with the deposition pressure, from 0.69 (2×10^{-3} Pa) up to 1.72° (5 Pa of He), indicating a reduction of the domain size. This is attributed to the confinement of the ablation plume leading to in-plume nanocluster nucleation and resulting in transition to a cluster-assembled growth regime of the film, as previously observed for metallic glasses [34] as well as W and W-Ta systems [40].

At the same time, the reflection corresponding to the (2 0 0) interplanar distance appears to be weak in the compact HEAs-TF suggesting partial texture. Finally, the HEAs-TF deposited by magnetron sputtering has a strong (1 1 1) texture, as shown by the presence of a single, strong peak at ~43° with a FWHM comparable to the instrumental broadening (0.22°). More details on the evolution of the FWHM for the (1 1 1) and (2 0 0) peaks are shown in Fig. S1.

Fig. 2 shows high angle annular dark field scanning transition electron microscopy (HAADF-STEM) characterization of compact and nanogranular HEAs-TF deposited by PLD, providing more information about their nanoscale features. HEAs-TF deposited at 2×10^{-3} Pa are composed of long nanocolumns oriented to the TF growth direction, with an average diameter of ~4.3 nm. This is due to the high energy and mobility of the ablated species upon landing on the substrate, which originate larger grains with a preferential orientation to minimize

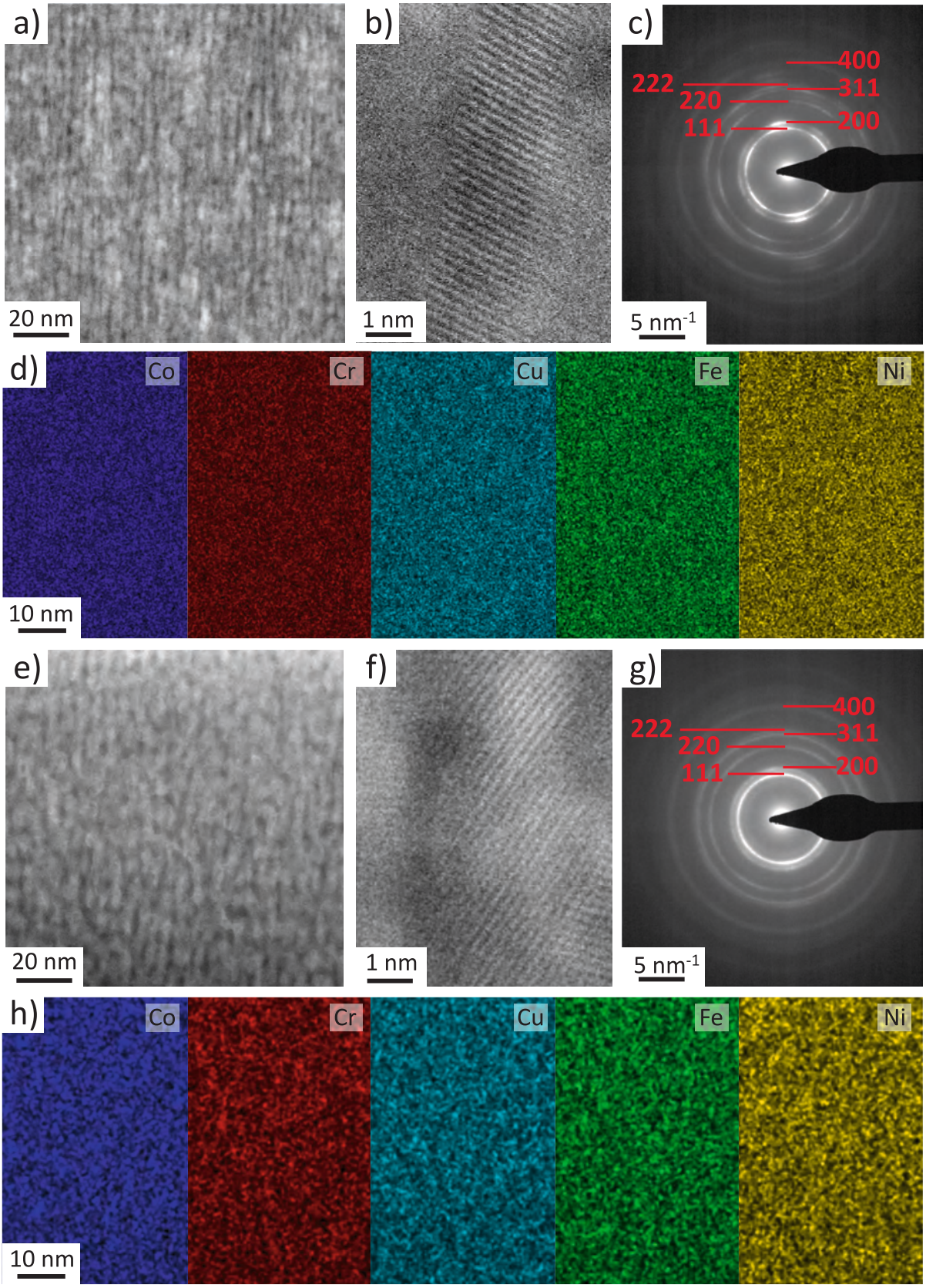

Fig. 2. HAADF-STEM micrographs of compact CoCrCuFeNi HEAs-TF deposited by PLD at 2×10^{-3} Pa (a), and nanogranular films with cluster assembled growth deposited at 5 Pa of He (e). Corresponding high magnification micrographs showing lattice fringes (b, f) and SAED patterns (c, g) with indexed diffraction rings for the FCC HEA phase. Compact HEAs-TF show a nanocolumnar structure and preferred orientation (see intensity reinforcement in SAED patterns), while nanoclustering without a specific preferred orientation can be observed for the nanogranular film. STEM-EDX mappings of the compact (d) and nanogranular (h) samples showing homogeneous elemental composition for both samples.

surface energy as shown by the strong (1 1 1) peak in XRD (Fig. 1d) and similarly to sputter-deposited TFs [41]. On the other hand, HEAs-TF deposited at 5 Pa show a nanogranular morphology with an average cluster diameter of 4.4 nm. This originates from the higher deposition pressure inducing in-plume cluster nucleation and the reduced energy and mobility of the nanoclusters upon landing on the substrate, resulting in a cluster-assembled film characterized by smaller domain/grains and reduced texture [32]. Furthermore, the EDX maps shows a homogeneous chemical composition without elemental segregation.

The selected area electron diffraction (SAED) patterns (Fig. 2c,g) confirm the presence of the FCC phase and match with the lattice plane spacing of the (1 1 1) and (2 0 0) reflection obtained by XRD (Fig. 1d). While bulk CoCrCuFeNi often contains a secondary FCC Cu-rich phase, resulting from the positive enthalpy of mixing of Cu with the other elements (+12 kJ/mol for Cr, +13 kJ/mol for Fe, +6 kJ/mol for Co, +4 kJ/mol for Ni) [38,39], such phase was not detected in PLD-deposited HEAs-TF as a result of the high cooling rates in PVD processes (vapor to solid) [30], inducing the stabilization of a an out-of-equilibrium single phase solid solution.

The preferential directions in the diffraction pattern can also provide information about grain orientation [42], confirming the partially oriented growth for compact HEAs-TF. On the other hand, the continuous rings in nanogranular HEAs-TF show that no oriented growth is present. This can also be inferred by the XRD data (Fig. 1d), in which the compact film shows a weaker (2 0 0) peak compared to the samples deposited at higher pressure, as a result of the randomly oriented nanoclusters upon landing on the substrate. For both cases, the discrete rings observed in the SAED are a further indication of the nanocrystalline structure of PLD-deposited HEAs-TF. Due to the ultrafine nanocrystalline nature of the HEAs-TF deposited by PLD, different grains can overlap throughout the lamella thickness, and lattice fringes cannot be easily observed by HRTEM. However, as shown in Fig. 2b,f, the smaller depth of field associated with the converged electron probe in HAADF-STEM allows to resolve the atomic lattice spacings of individual grains (additional micrographs are available in Fig. S4). The measured interplanar spacing is ~2.06 Å, an expected value for the (1 1 1) FCC HEA phase and in agreement with the XRD data shown in Fig. 1d.

Fig. 3a shows structural features of HEAs-TF deposited by PLD at different background gas pressure to better investigate the transition from compact to nanogranular morphology and the effect of nanoclustering, while comparing with the properties of magnetron sputtered TFs. The average crystallite size measured from Scherrer's equation (along the growth direction) decreases from 38.5 ± 1.5 down to 11.2 ± 0.6 nm as the background pressure increases as a result of nanoclustering during the deposition process. This reduction was also observed by TEM characterization (Fig. 2a,e), while also highlighting a much smaller width of 4.3 ± 1.3 nm for the compact film. On the other hand, sputter-deposited HEAs-TF report columnar grains with an average diameter of 42 ± 6 nm and height corresponding to the film thickness (≈880 nm) as observed from SEM characterization (Fig. 1c), a common feature of crystalline TF deposited by sputtering.

Fig. 3b reports the mass density evolution extracted by X-Ray reflectivity (XRR). It shows that compact HEAs-TF deposited by PLD have the highest mass density, differing only by ~6% from the ideal value expected from this alloy (8.22 g/cm^3, see Section S2 of the supplementary material). The ~15% reduction in mass density when the deposition pressure increases above 0.1 Pa (He) can be attributed to the reduction of the plasma plume size, promoting in-plume cluster nucleation and cluster-assembled growth [41]. Moreover, compact HEAs-TF (2×10^{-3} Pa) exhibit higher mass density vs sputter-deposited counterparts as result of the highest energy involved in the PLD process (vs magnetron sputtering) and the lower deposition pressure.

Electrical resistivity measurements have been carried out to explore the transition from compact to nanogranular film as a function of the deposition pressure (Fig. 3c). The nanogranular morphology shows a significant increase of resistivity (282 μΩ×cm), compared to the HEAs-TF prepared in vacuum (139 μ×cm). This is attributed to an increase in scattering events at the grain boundaries due to the smaller domain size and nanoclustering [43]. On the other hand, sputter-deposited films show the lowest resistivity (102 μΩ×cm) due to the larger grain size (42 nm) along the direction of current flow, namely the plane perpendicular to the growth direction. These values are higher than the resistivity of 57 μΩ×cm reported for coarse grained CoCrCuFeNi [44] due to the difference in grain size, although the presence of Cu dendrites commonly observed in bulk CoCrCuFeNi might be another factor decreasing resistivity.

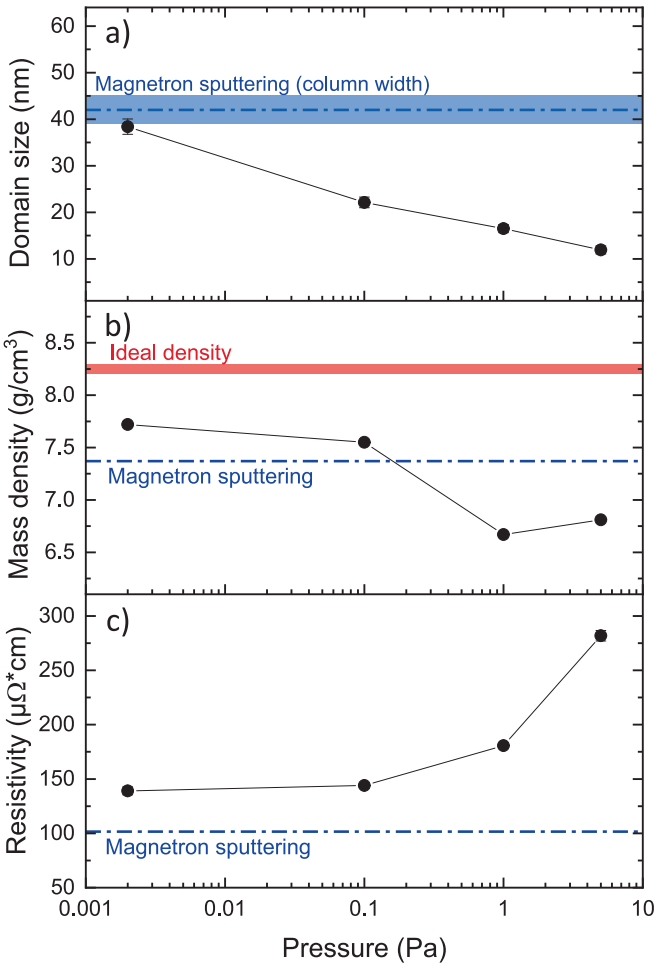

Fig. 3. a) Domain size from XRD, b) Mass density from XRR, c) Electrical resistivity of CoCrCuFeNi HEAs-TF by PLD as a function of background pressure, showing how the transition from compact to nanogranular morphology affects structural properties. The blue horizontal lines represent the values for the sputter-deposited film.

Microscale mechanical behavior for as-deposited HEAs-TF

The elastic and plastic properties of the as-deposited HEAs-TF by PLD and magnetron sputtering have been investigated by nanoindentation, optoacoustic techniques and micropillar compression, as shown in Fig. 4. The measured elastic modulus for the PLD deposited CoCrCuFeNi samples matches with literature results from both molecular dynamics simulations and experimental values of the bulk alloy (~175 GPa) [45,46].

The high elastic modulus (E) observed for the HEAs-TF deposited by magnetron sputtering (203 GPa by nanoindentation) – which is 30 GPa higher than PLD-deposited counterparts (173 GPa) – originate from the strong (1 1 1) texturing, combined with the high elastic anisotropy of

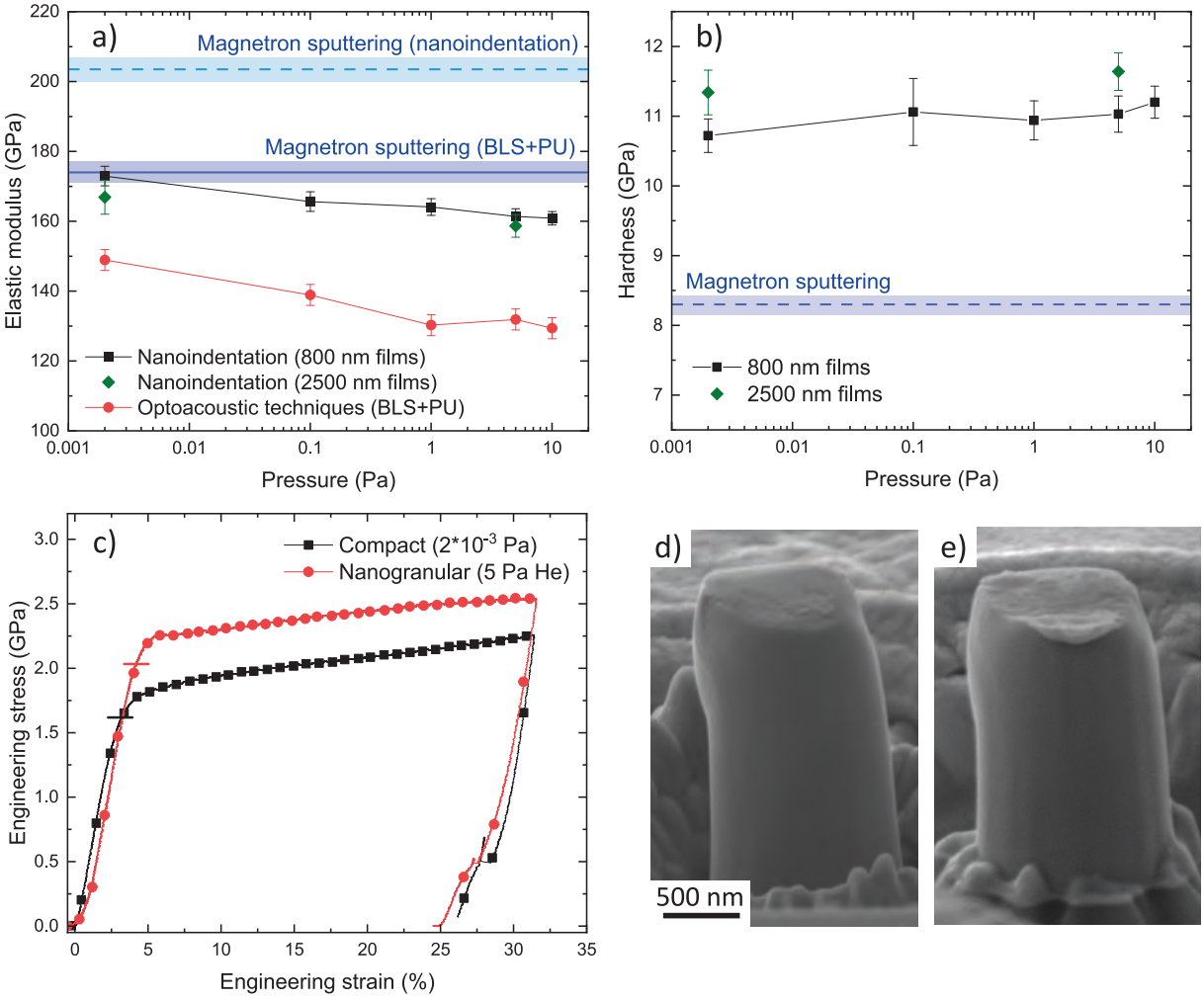

Fig. 4. Mechanical properties of CoCrCuFeNi HEAs-TF deposited by PLD at different background pressures and with different thicknesses compared to magnetron sputtering counterparts. a) Elastic modulus by nanoindentation and optoacoustic techniques. A reduction of E for nanogranular films due to nanoclustering can be observed as well as the higher E for (1 1 1) textured film synthesized by magnetron sputtering. b) Hardness, showing how the nanosized grains in PLD deposited HEAs-TF lead to larger values of H. c) Stress–strain curves during micropillar compression of HEAs-TF by PLD, showing high yield strength and plasticity without crack formation up to 30% strain, resulting from the ultrafine grains and unique nanoscale features. The horizontal bars mark the 2% deviation from the elastic regime. d, e) Post mortem SEM images of micropillars after compression up to 30%, for respectively, HEAs-TF deposited at 2×10^{-3} Pa and 5 Pa He.

FCC HEAs, as previously reported in literature [47]. More specifically, PLD-deposited HEAs-TF have randomly oriented grains and can be approximated to an isotropic system, while the textured magnetron sputtering TFs have different elastic properties depending on the direction (parallel or perpendicular to the film growth). This was confirmed by recreating the full stiffness matrix from optoacoustic measurements, as well as using the Voigt-Reuss-Hill method starting from the ideal single crystal elastic constants, see more detail in section S3.

From Fig. 4a, it can also be observed that the elastic modulus of HEAs-TF deposited by PLD slightly decrease as the deposition pressure increases, as confirmed both by nanoindentation and optoacoustic techniques. As a matter of fact, the reduction of both mass density and domain size results in a significant fraction of atoms belonging to grain boundaries, reducing the average bond strength [48].

Fig. 4b reports the evolution of hardness (H) extracted by nanoindentation as a function of the background gas pressure during PLD depositions in comparison with sputter-deposited counterparts. HEAs-TF produced by PLD possess constant $H \sim 11$ GPa regardless of the background pressure, ~32% higher than sputter-deposited counterparts ($H = 8.3$ GPa). This can be attributed to their ultrafine grain structure, leading to Hall-Petch strengthening, as confirmed by atomistic simulation studies on this HEA system [49] showing Hall-Petch strengthening occurring for grains sizes as small as ~12 nm. Thicker films (2500 nm) were also tested to exclude any effect of the presence of a hard substrate ($E \sim 170$ and $H \sim 12$ GPa for Si, respectively) during the measurement. No significant difference was found either for E or H for the 2500 nm HEAs-TF (see Fig. 4a,b), confirming as well that the growth mechanisms and the mechanical behavior are not affected by the film thickness, and result from Hall-Petch strengthening.

Fig. 4c-e shows micropillar compression tests of compact and nanogranular PLD-deposited HEAs-TF in order to explore the mechanical behavior under uniaxial loading, while obtaining the stress–strain curve and investigating the deformation behavior. Compact HEAs-TF show a yield strength (σ_y) equal to 1.62 ± 0.05 GPa. This value is outperformed by the nanogranular HEAs-TF with σ_y reaching 2.03 ± 0.07 GPa, a 25% increment, due to the smaller grain size along the direction of applied stress. For comparison, the σ_y for single crystal CoCrCuFeNi micropillars with comparable micropillar geometry is only 0.45 GPa [50], where the main source of strengthening comes from weak Peierls stresses (<100 MPa for FCC HEAs [27]). The Hall-Petch strengthening is evident in both nanoindentation and micropillar compression experiments. However, the distinct TF's morphologies produced by PLD result in different trends between nanoindentation hardness (constant ~11

GPa) and micropillar compression (which show a higher yield strength for the nanogranular HEAs-TF). This can be explained by the different loading configuration and microstructure of HEAs-TF. Specifically, micropillar compression tests apply stress primarily along the vertical direction, while nanoindentation induces a more complex, multidirectional stress field [51]. Additionally, the compact HEAs-TF films exhibit anisotropic grain sizes, with smaller grains in the lateral direction (~4.3 nm) compared to the vertical. In contrast, nanogranular HEAs display an isotropic grain structure with uniformly small grains (~4.4 nm), as shown in Fig. 2. Consequently, the H measured by nanoindentation is influenced by the smallest grain dimension, accounting for the plateau observed in Fig. 4b. Meanwhile, the nanogranular HEAs-TF, with significantly smaller vertical grain sizes than the compact films, exhibit higher yield strengths when tested via micropillar compression.

At the same time, micropillar compression tests show high plastic deformability even after 30% strain, as expected from FCC HEAs due to their inherent strong ductility [52], and no clear slip planes or fractures are visible in the *post mortem* SEM images. Finally, apparent strain hardening observed in micropillar compression can be explained by the increase in the micropillar diameter during compression resulting from both plastic and elastic deformation.

Thermal stability

Fig. 5 reports *in situ* XRD annealing experiments over a temperature range up to 610°C, enabling to monitor the growth process of crystallite domains, while evaluating the thermal stability. Moreover, this enables to select precise post-thermal annealing conditions capable to tune grain size of PLD-deposited HEAs-TF, tailoring the mechanical properties and evaluating Hall-Petch relationship. Compact HEAs-TF are thermally stable up to 370°C with the absence of phase segregation and oxides formation. Then, the FWHM corresponding to the (1 1 1) peak decreases starting at 370°C indicating an increment of domain size, followed by the appearance of a new diffraction peak at 45° (Fig. 5a). As the temperature increases to 610°C, the presence of a trigonal Cr_2O_3 phase [53] can be observed, similarly to previous findings during the annealing of CoCrFeNi [54]. The same secondary phases can be observed during annealing of nanogranular HEAs-TF (Fig. 5b), with the FWHM of the (111) peak decreasing starting from 400°C. However, in this case, the diffraction peaks of the secondary phases appear more evident due to the weaker diffraction peaks of the FCC HEA. The two reflections at 45 and 65° are consistent with a BCC phase with a lattice parameter of 2.87 Å, in agreement with *in situ* TEM annealing of CoCrCuFeNi by Arfaoui *et al.* [55]. Furthermore, this secondary phase has a similar lattice parameter with a BCC Fe_xCu_y metastable phase, which has been occasionally observed in Cu-containing steels [56]. In this case, the segregation of a Cu-containing secondary phase is supported by its positive enthalpy of mixing with respect to the other elements, as discussed in section 2.1.

Fig. 5c shows the evolution of domain size extracted using Scherrer's equation from the (111) peak of the HEA phase as a function of temperature, highlighting the different thermal stability between the PLD-deposited HEAs-TF. Starting from T_{room}, the domain size of the compact TFs remains unchanged until 370°C, after which the process of grain growth begins. The grain size in compact HEAs-TF reaches a plateau ~ 55 nm at ~ 460°C, increasing again starting from 550°C. On the other hand, nanogranular HEAs-TF maintains a lower domain size compared to the compact counterparts until annealing at 610°C and showing a delayed onset of grain growth (400°C). While bulk HEAs typically have higher thermal stability as a result of their random atomic distribution, our results show that nanogranular PLD-deposited HEAs-TF are able to maintain a high thermal stability despite the nanosized grains compared to the coarser grained compact counterpart, with an onset of grain growth of ~ 49% T_m, with $T_m = 1100$°C for CoCrCuFeNi [57]. The lower grain size of the nanogranular TFs compared to the compact counterpart at $T < 580$°C can be explained by the nanoclustered structure, providing an even stronger barrier to grain growth.

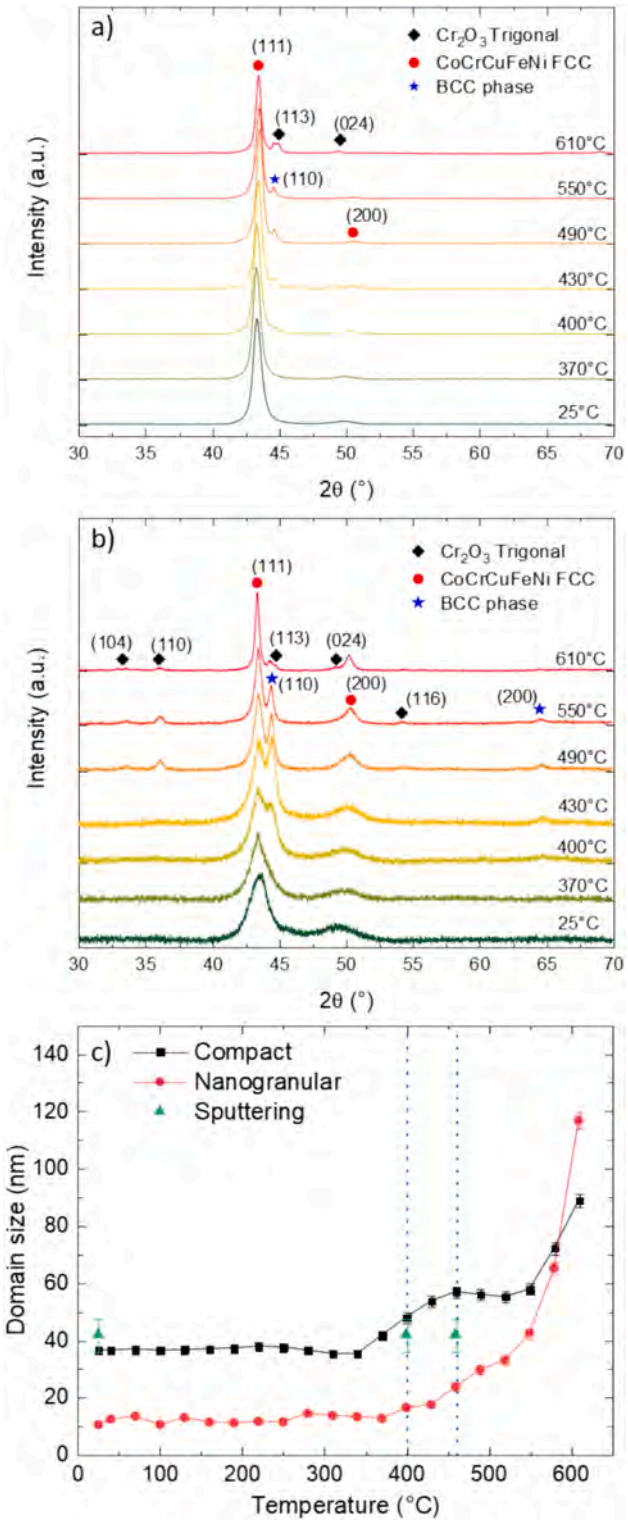

Fig. 5. Evolution of the microstructure of CoCrCuFeNi HEAs-TF deposited by PLD during *in situ* XRD heating experiments. Diffractograms of compact (a) and nanogranular (b) films taken at different temperatures show the reduction of FWHM for the (1 1 1) peak and segregation of secondary phases as the temperature increases. c) Evolution of the domain size for HEAs-TF obtained from (1 1 1) FCC peak using Scherrer's equation as a function of temperature. The domain size for HEAs-TF deposited by magnetron sputtering refers to the width of the columns which are not affected by the annealing treatment. The vertical dotted lines represent the temperatures that were chosen for ex situ annealing in order to further study the grain growth process.

Based on *in situ* XRD annealing results, HEAs-TF synthetized by both magnetron sputtering and PLD were annealed at 400 and 460°C for 1 h in order to induce grain growth and to investigate the evolution of microstructural features and mechanical behavior. This choice has been also dictated to reduce the effect of oxidation and to limit the formation of secondary phases. Fig. 6a shows the evolution of hardness (*H*) for all HEAs-TF, which is mostly unaffected after annealing at 400°C. This is consistent with the results from *in situ* XRD since the grain growth process is still at an early stage (average domain size equal to 16 and 47 nm for nanogranular and compact HEAs-TF respectively). Furthermore, the formation of the hard BCC secondary phase does not show a significant impact on mechanical properties, suggesting that the mechanical behaviour is primarily governed by the grain size. On the other hand, the *H* of PLD deposited HEAs-TF decreases after annealing at 460°C to 9.0 and 7.7 GPa for the nanogranular and compact films, respectively. As shown from Fig. 5c, nanogranular HEAs-TF are able to maintain a smaller domain size compared to the compact counterparts during annealing at 460°C, resulting in higher hardness due to Hall-Petch strengthening.

Finally, the HEAs-TF deposited by magnetron sputtering do not experience grain growth after annealing at 460°C due to the larger grain size (vertical size equal to film thickness) and lower density of grain boundaries. As a result, any grain growth is constrained and can occur only in the direction perpendicular to the film growth. As a consequence, the hardness remains mostly unaffected after annealing (8.0 GPa), and is close to the values of the annealed compact HEAs-TF by PLD due to the similar domain size (57 and 46 nm, respectively), Fig. 5c.

Fig. 7 shows STEM characterization of the HEAs-TF annealed at 460°C, revealing a heterogeneous chemical composition. The SAED rings for both compact and nanogranular HEAs-TF are not continuous and individual diffraction spots are visible, suggesting an increase in grain size compared to the as- deposited films shown in Fig. 2c,g. While the HAADF-STEM images in Fig. 7 mainly highlight the chemical (Z) contrast, revealing compositional variations and possible phase segregation, the bright field TEM micrographs in Fig. S5 predominantly exhibits diffraction contrast, qualitatively showing the grain growth of the annealed HEAs-TF. The corresponding STEM-EDX elemental maps unveil local segregations which are consistent with *in situ* XRD data (Fig. 5). The even distribution of O on HEAs-TF observed mostly for compact films (Fig. 7b) can be explained by the difficulty of accurately measuring low Z elements by STEM-EDX, in combination with the surface oxidation with TEM lamella preparation. Moreover, as previously studied by Lee *et al.* [58], a spinel high entropy oxide phase should be thermodynamically favored for HEAs within the Cantor family. However, the formation of trigonal Cr_2O_3 is kinetically favored, and can even passivate the HEA at more advanced stages of oxidation. A high entropy oxide spinel phase was not detected as confirmed by analyzing the SAED of the annealed HEAs-TF (Table S1), where the diffraction rings correspond only with the FCC HEA phase, the secondary BCC phase and trigonal Cr_2O_3, in agreement with XRD characterization (Fig. 5). Finally, Fig. 7 displays the presence of Cu-rich regions corresponding to the BCC phase, which are expected due to the positive enthalpy of mixing of Cu compared to the other elements [59]. Interestingly, a self-assembled nanolaminate structure is observed for the annealed nanogranular HEAs-TF with Cr_2O_3 rich layers and a bilayer period of ~50 nm, as shown in Fig. 7d. This morphology is similar to previously reported nanogranular metallic glasses deposited by PLD [60], and can be explained by the higher density of grain boundaries favoring the diffusion of O.

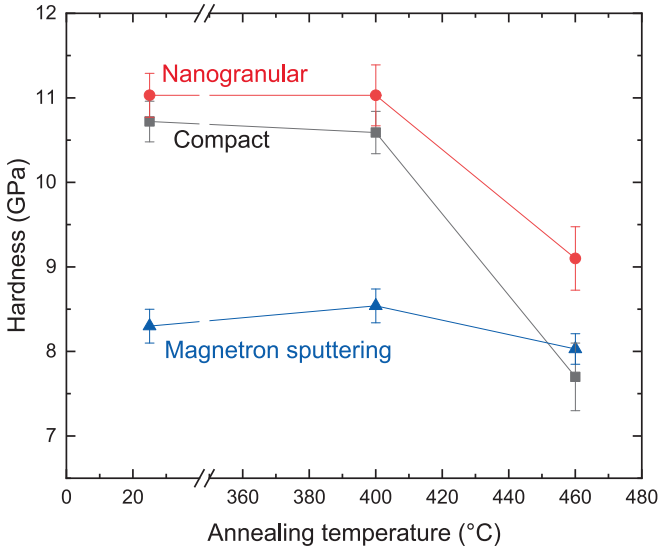

Fig. 6. Evolution of hardness of CoCrCuFeNi HEAs-TF deposited by PLD and magnetron sputtering as a function of annealing temperature, highlighting the influence of microstructure on thermal stability.

Discussion

In the previous sections, we show the potential of PLD to fabricate unique TF with ultrafine grain structure, controlling the background gas pressure to induce in-plume cluster nucleation, and the following cluster-assembled growth regime [61]. This results in TFs with high density of nanointerfaces and/or grain boundaries, as previously shown for metallic glasses [34] as well as W and W-Ta systems [40]. This approach has been extended here to synthetize ultrafine FCC multicomponent alloys, significantly enhancing both the mechanical properties and the thermal stability. Furthermore, the extremely out-of-equilibrium conditions of PLD [30], with the average energies of ablated species up to 100 eV [31], an order of magnitude above sputtering (usually <15 eV, with a fraction of these atoms reaching the target at <0.05 eV [28]) promote the stabilization of a single-phase HEAs-TF with high mass density vs the sputter-deposited one (Fig. 3b). This factor, in combination with the ultrafine grain size, results in higher hardness and yield strength values up to 11 and 2.0 GPa respectively.

To put the previous studies in a more general context, Fig. 8 compares the mechanical properties and thermal stability of the HEAs-TF from this work to other literature results. Fig. 8a shows the *H* of different FCC HEAs of first group transition metals with a lattice distortion comparable to that of CoCrCuFeNi ($\delta \sim 1\%$) [17,18,38,62–68], highlighting the Hall-Petch dependence for different domain sizes. Starting from the coarse-grained bulk HEAs, *H* increases from values as low as ~2.5 GPa roughly following a linear trend with respect to $d^{-1/2}$, where *d* is the domain size, as expected from the Hall-Petch strengthening regime. This strengthening effect reaches it ceiling values for the ultrafine HEAs-TF deposited by PLD, with a plateau of hardness at 11 GPa for a domain size < 38 nm.

Nanocrystalline HEAs-TF synthetized by sputtering with a grain size <20 nm have been reported in literature [38]. However, these TFs present a much lower *H* (<9 GPa) compared to the PLD-deposited counterparts. This is due to the specific sputtering parameters required to synthetize nanocrystalline TFs, resulting in a high nanoporosity content induced by the low energy of the sputtered species (zone I of the Thornton diagram [41]). This counteracts the Hall-Petch strengthening effect [38], leading to a decrement of *H*. In another study, Xiao *et al.* [68] demonstrated that thermal annealing of sputter-deposited HEAs-TF can stabilize the grain boundaries of dual phase CrMnFeCoNi TFs, leading to high *H* (up to ~13.8 GPa Furthermore, dense TFs can be obtained by magnetron sputtering, and a careful design of the HEA can still result in high *H*. As an example, Liao *et al.* [69] synthesized $CoCrFeNiAl_{0.3}$ TFs, with *H* up to 12.3 GPa due to the presence of FCC and BCC nanocrystals.

These results are supported by atomistic simulation studies from Zhang and Shibuta [49], reporting positive Hall-Petch effect for CoCrCuFeNi until the grain size is 18 nm, followed by a transition to an

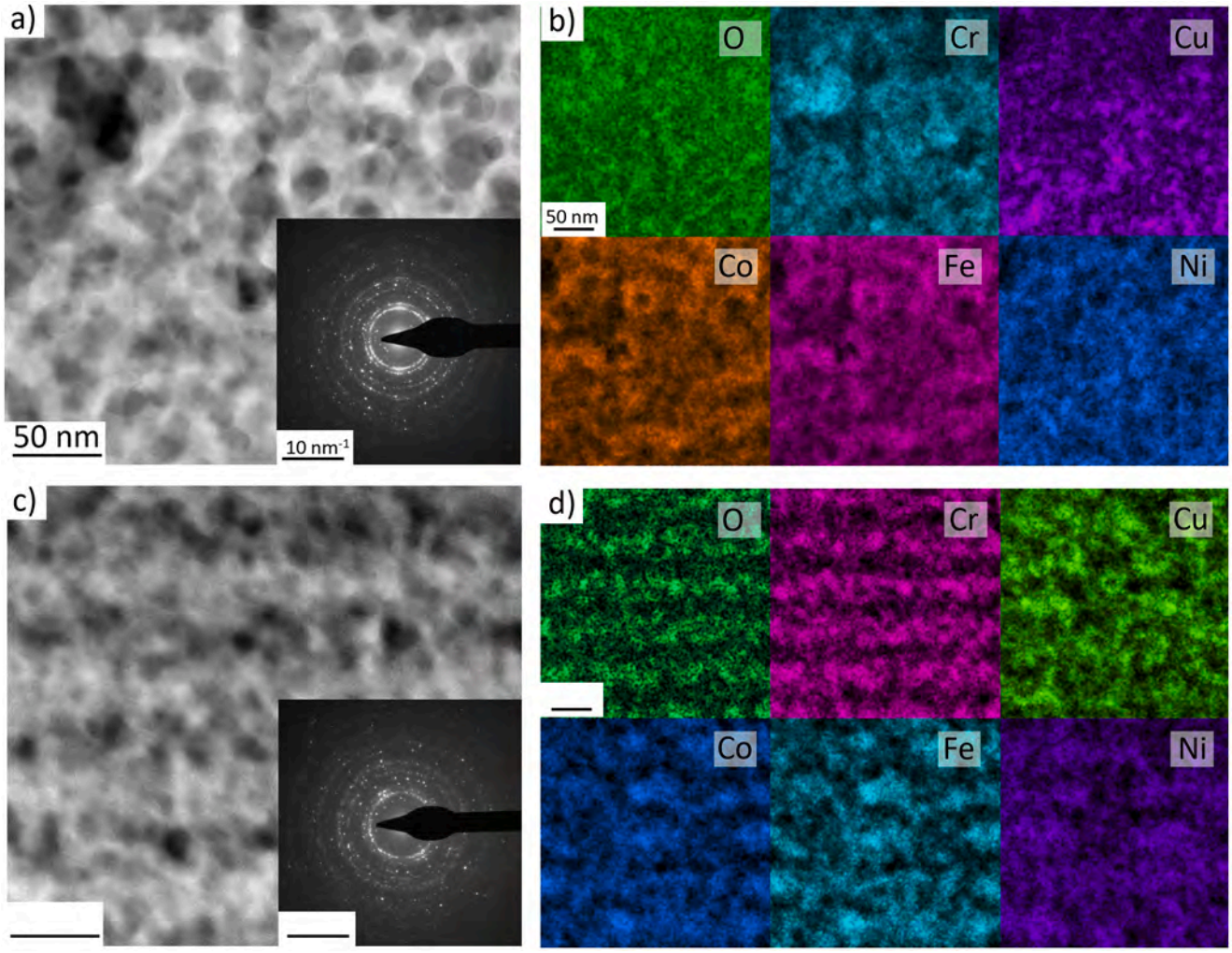

Fig. 7. High resolution HAADF-STEM cross section of compact (a) and nanogranular (c) HEAs-TF after 1 h of annealing at 460°C, with corresponding SAEDs (insets) and corresponding EDX mappings (b, d). A complex elemental nanosegregation can be observed for both samples, while layers with higher concentration of Cr and O are visible for the nanogranular HEAs-TF. Scale bars are the same for each set of images.

inverse Hall-Petch regime for grain sizes below ~12 nm. The plateau predicted between these two regimes corresponds to the PLD deposited films presented in this work, and it represents the highest strength that can be achieved through the Hall-Petch effect. The large plasticity of HEAs, especially in compression, has been observed in literature for FCC bulk HEAs [6], reporting up to 90% plastic deformability. However, our results have shown that a large plasticity can be found even in ultrafine nanocrystalline HEAs-TF. This is in agreement with atomistic simulations [49], where it was shown that the deformation of nanocrystalline CoCrCuFeNi is mediated by enhanced grain boundary activity, such as stress induced grain boundary migration. Moreover, the same work reports that dislocation-based mechanisms (stacking faults, twinning) have a key role as well in enhancing plasticity in nanosized grains alloys, suggesting a complex interplay between the deformation modes. The ultrafine HEAs-TF can thus benefit of both deformation mechanisms, resulting in large plasticity in compression without failure up to 30% of strain. Moreover, the cluster-assembled microstructure can enable micro and nanoscale stress accommodation resulting in another contributing factor explaining for the large plasticity of nanogranular HEAs-TF, similarly to what has been reported even for intrinsically brittle materials such as metallic glasses [34].

Fig. 8b compares the thermal stability – defined as the onset temperature of grain growth normalized to the melting temperature (T_m) – of PLD deposited HEAs-TF (this work) with different FCC metals as a function of their grain size [55,70–77]. It is known that thermal stability worsens when the grain size approaches the nanoscale due to the higher density of grain boundaries, with an extreme example being nc Cu, where grain growth can begin at temperatures as low as ~20% T_m [71]. The HEAs-TF deposited by PLD are able to maintain a larger thermal stability with structural variation occurring at T/T_m equal to 49% and 47% respectively for compact and nanogranular films. This result is in line with sputter-deposited HEAs-TF with domain size equal to ~100 nm [55], while being lower than those reported for bulk HEAs with micrometer sized grains and similar composition [63] due to increased density of grain boundaries. However, despite their nm size grains, ultrafine HEAs-TF are able to maintain a larger thermal stability compared to elemental metals with comparable grain size (T/T_m = 40% and 20% for, respectively, Ni and Cu [71,73]). This can be attributed firstly to the general features of HEAs such as the sluggish diffusion effect which reduces atomic mobility [78], as well as the distorted lattice structure which results in a smaller difference in Gibbs' free energy between the crystalline phase and the grain boundaries compared to traditional metals [25] and therefore retaining higher thermal stability with higher onset temperature for grain's growth.

Conclusions

In this work, we exploit the potential of Pulsed Laser Deposition

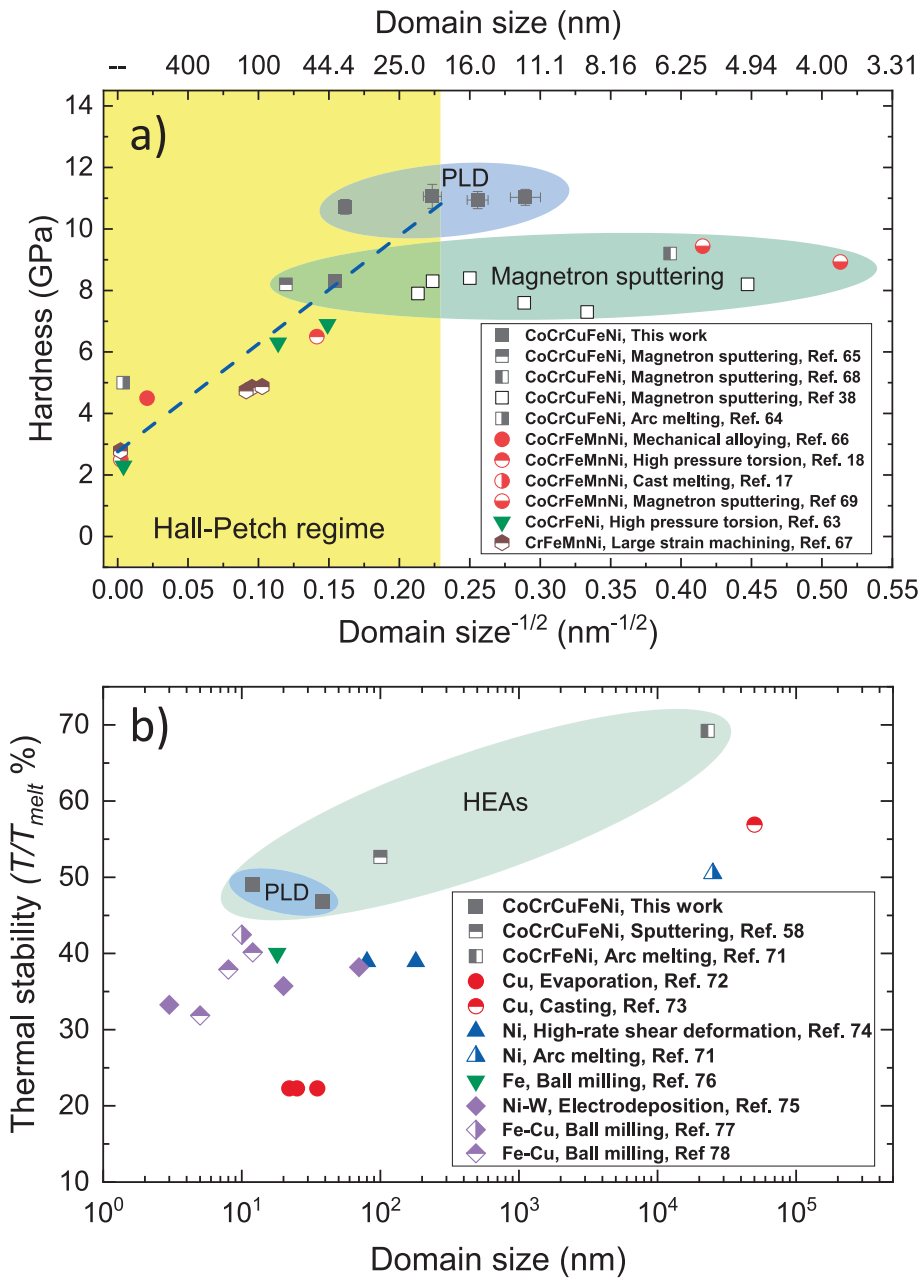

Fig. 8. a) Hardness of different FCC HEAs as a function of domain size. The blue dashed lines represent the average trend, highlighting the Hall-Petch regime, followed by the onset of the inverse Hall-Petch effect. PLD-deposited HEAs-TF show higher hardness as a result of their ultrafine structure triggering Hall-Petch strengthening b) Thermal stability of different FCC metals normalized with respect to their melting point as a function of domain size.

(PLD), providing a novel pathway to easily synthetize ultrafine and dense FCC CoCrCuFeNi HEAs-TF, resulting in a superior combination of strength-plasticity-thermal stability. Moreover, we carried out a multi-scale investigation of mechanical properties and thermal stability investigating the relationship with the atomic and microstructure. The main findings of this work are:

- PLD can be used to produce ultrafine HEAs-TF, controlling both the microstructure and the domain size by simply adjusting the background pressure. Specifically, compact films (with domain size equal to 36 nm) are synthetized at 2×10^{-3} Pa, while increasing the pressure (5 Pa of He) yields nanogranular films with smaller domain size (12 nm) as a result of the transition from atom-by-atom to a cluster-assembled growth mechanism.
- High hardness (~11 GPa) and yield strength (up to 2 GPa) was reached for PLD-deposited FCC HEAs-TF. Such outstanding values are significantly higher than previous reported data of similar FCC HEAs from literature, as a result of Hall-Petch strengthening due the ultrafine nanostructure. Moreover, micropillar compression tests still show high plastic deformability up to 30%.
- Despite the small grain size, ultrafine HEAs-TF deposited by PLD exhibit grain/domain growth starting from $T > 400$°C, corresponding to 49% of T_m, highlighting the higher thermal stability of HEAs-TF with respect to conventional metals and alloys with similar grain size. Further increment in temperature at 460°C results in grain growth (up to 57 nm) and lower hardness, reaching values of sputtered-deposited HEAs-TF with similar grain size (42 nm). Moreover, nanogranular HEAs-TF have higher thermal stability and

are capable to maintain smaller grain size after annealing at 460°C, resulting in a higher hardness (9.1 GPa).

Overall, in this study we show the synthesis of a new class of HEAs-TF with mutual combination of mechanical properties and thermal stability, overcoming the traditional trade-off between strength, ductility and thermal stability and opening up a new approach which can be extended to other class of metallic materials.

Methods

Synthesis of nanostructured CoCrCuFeNi HEAs-TF

The CoCrCuFeNi HEAs-TF have been synthetized by magnetron sputtering and pulsed laser deposition (PLD) starting from 2 inch arc-melted CoCrCuFeNi targets (purity >99.99%) on Si (1 0 0) substrate. In PLD experiments, the target was ablated using a Nd-YAG laser with a pulse length of 5–7 ns, a wavelength of 532 nm (2^{nd} harmonic) and a pulse frequency of 10 Hz. The energy of each pulse was constant and equal to 610 ± 10 mJ, and the optics were set up to have a fluence of 31 mJ/mm^2 on the target. Prior to deposition, the base pressure was set <2 × 10^{-3} Pa and the target was cleaned by laser ablation for a duration >5 min to remove surface contamination, while the substrate was covered by a shutter. For samples that required a higher background pressure, He gas was pumped in the chamber with a PID controlled valve reaching 0.1, 1, 5 and 10 Pa in order to induce a transition from atom-by-atom to cluster-assembled growth [79]. The target-substrate distance was equal to 70 mm for all depositions, and the growth rate was around 25.5 nm/min. Depositions using magnetron sputtering were carried out at T_{room} under a deposition pressure of 0.5 Pa, using Ar gas with a flow rate of 40 sccm. These parameters were selected in order to compare with the PLD-deposited HEAs-TF, while reflecting standard sputtering deposition conditions to enable comparison with other literature studies [80]. Prior to deposition, a base pressure <7 × 10^{-5} Pa was reached ensuring no external contamination. An RF power supply was used, applying 200 W to the HEA target for all depositions, while the target-substrate distance was set to 90 mm. The growth rate was measured (29.3 nm/min) to obtain films with 800 nm thickness. The thickness of 800 nm was chosen for all HEAs-TF by both PLD and magnetron sputtering as a good balance for probing the mechanical properties by nanoindentation – requiring a larger thickness to minimize the influence of the substrate [81] – and by optoacoustic techniques, which provide higher quality data for films with lower thickness (usually < 1 μm) [82].

Investigation of grain growth by post-thermal annealing treatments

In situ high temperature X-ray diffraction (XRD) experiments have been carried out to study the grain growth and thermal stability. Measurements were acquired in steps of 30°C, while operating in a He atmosphere to limit oxidation. The heating rate was set to 30°C/min, while the cooling rate was 10°C/min. The maximum annealing temperature for these samples was 610°C, due to the difference in thermal expansion coefficients between the samples and the Si substrate causing delamination. A second batch of samples were then annealed in a vacuum furnace at 400 and 460°C for one (1) hour with a heating and cooling rate respectively of 20 and 10°C/min similarly to *in situ* XRD experiments, while enabling to study the evolution of microstructure and mechanical behavior. The thermal stability (T/T_m) was defined as the ratio between the onset temperature of grain growth (T) and the melting temperature (T_m) of that alloy.

Elemental, microstructural and electrical characterizations

The microscale morphology and the elemental composition of different HEAs-TF samples before and after thermal treatments have been investigated using a scanning electron microscope (SEM) Supra 40VP paired with a Bruker energy dispersive X-ray spectrometer (EDX). The cross sections were imaged using an accelerating voltage of 5 kV and a working distance equal to 3 mm, while the EDX data were acquired at 15 kV at and optimal working distance equal to 8.5 mm. The chemical composition of all the samples is presented in Table S2.

The structural characterization has been performed by XRD and X-ray reflectivity (XRR). XRD experiments were carried out with a Rigaku Smartlab diffractometer equipped with a CuK_α source (λ = 1.5406 Å) in Bragg-Brentano geometry with a resolution of 0.01° and an offset of 3° to remove the signal from the substrate. Scans were carried out within a 2θ interval from 30 to 80°. The peaks were fitted with a Voigt function to obtain the peak position and FWHM, which has been exploited to extract the lattice parameter, as well as the domain size (d) using Scherrer's equation [83] as follows:

$$\boldsymbol{d} = \frac{\boldsymbol{K}^*\lambda}{\cos(\theta)^*\boldsymbol{FWHM}}$$

where λ is the XRD wavelength, K is Scherrer constant (~0.9), and θ refers to the peak position. XRR data was obtained using a Seifert XRD 3000 diffractometer operating at 40 kV and 40 mA using a Cu K_α source. To measure the critical angle (θ_{crit}) and obtain the mass density of HEAs-TF, scans were performed between 0.2° and 2.5° with a step of 0.05°. More details about this method can be found in the supplementary material.

The nanoscale characterization has been performed by cross-sectional transmission electron microscopy (TEM) with specimens prepared by Focused Ion Beam (FIB) with an FEI Strata 400S dual beam SEM/FIB. TEM and selected area electron diffraction (SAED) images were acquired in a Cs- double corrected Thermo Fisher Titan Themis Z operated at 300 kV using the Gatan OneView CMOS camera. Scanning TEM (STEM) images and STEM-EDX were conducted in a Cs- probe corrected Thermo Fisher Titan Themis 60–300 operated at 300 kV using a semi-convergence angle of 30 mrad. The microscope is equipped with the ChemiSTEM SuperX EDS detector. For imaging, the high-angle annular dark-field detector was used at a camera length of 100 mm.

Electrical resistivity measurements were carried out to gain information on grain boundary scattering of electrons and density of interfaces. The samples were probed using 4 tungsten needles in a LINKAM-HFS600, and the electrical resistivity was measured using the standard Van der Pauw method, correcting for any asymmetries in the sample shape or probe position [84].

Micro-mechanical characterization

A KLA G200 nanoindenter equipped with a DCM head and a diamond Berkovich tip was used for nanoindentation measurements. All indentations were performed in continuous stiffness measurement (CSM) mode, obtaining hardness and elastic modulus as a function of depth [85]. The indentations were performed up to 400 nm with a maximum allowed drift rate of 0.05 nm/s and target strain rate of 0.05 s^{-1}. To minimize substrate contribution, the average hardness and elastic moduli were measured at low indentation depths to avoid influence of the substrate, as shown in Fig. S6.

The elastic properties have been measured using optoacoustic techniques, namely Brillouin light scattering (BLS) and picosecond laser ultrasonics (PLU). For BLS measurements, the sample was illuminated by a 532 nm laser with average power of 200 mW and an incident angle of 65°. The backscattered inelastic light was analyzed by a Sandercock tandem Fabry-Perot interferometer. PLU uses a pump/probe system composed of a 400 nm probe and an 800 nm pump beams. The combination of these two techniques allowed for the extraction of the full stiffness matrix, and a detailed explanation is provided in the supplementary material.

Micropillar compression tests were carried out on 2500 nm thick HEAs-TF using a Bruker Hysitron PI88 SEM PicoIndenter equipped with a diamond flat punch tip (3 μm diameter) with a constant displacement

rate of 9 nm/s. In order to mill the pillars, an Auriga Ga FIB was used with a voltage of 30 KV, taking 3 separate steps with progressively smaller current and diameter. All pillars have an aspect ratio of ≈2.5, with a taper angle <5°, and 6 pillars were tested for each sample to ensure repeatability.

CRediT authorship contribution statement

Davide Vacirca: Writing – original draft, Methodology, Investigation, Formal analysis, Data curation. **Francesco Bignoli:** Writing – review & editing, Methodology, Investigation. **Andrea Li Bassi:** Writing – review & editing, Validation, Resources. **Yuting Dai:** Writing – review & editing, Investigation. **Ali Ahmadian:** Writing – review & editing, Methodology, Investigation. **Gregory Abadias:** Writing – review & editing, Methodology, Investigation. **Philippe Djemia:** Writing – review & editing, Methodology, Investigation. **Gerhard Dehm:** Writing – review & editing, Validation, Resources, Methodology. **James P. Best:** Writing – review & editing, Validation, Supervision, Resources. **Matteo Ghidelli:** Writing – review & editing, Validation, Supervision, Resources, Project administration, Funding acquisition, Conceptualization.

Declaration of competing interest

The authors declare that they have no known competing financial interests or personal relationships that could have appeared to influence the work reported in this paper.

Acknowledgments

M. Ghidelli and D. Vacirca acknowledge the main financial support of the ANR JCJC project "Micro-HEAs" (grant agreement no. ANR-21-CE08-0003-01) as well as the CNRS-MPG (Max Planck Gesellschaft) program "SALTO" (project "NanoInt-HEAs") funding the mobility between the Laboratoire des Sciences des Procédés et des Matériaux (LSPM) and the Max Planck Institute for Sustainable Materials (MPI-SusMat). M. Ghidelli also acknowledges the support from the ANR projects “EGLASS” (grant agreement no. ANR-22-CE92-0026-01) and "Super-Glasses" (grant agreement no. ANR-24-CE91-0002-02). The authors acknowledge B. Breitbach and L. Belliard for support on XRD characterization and optoacoustic techniques, respectively. This work was partly carried out with the support of the Karlsruhe Nano Micro Facility (KNMF, www.knmf.kit.edu), a Helmholtz Research Infrastructure at Karlsruhe Institute of Technology (KIT, www.kit.edu).

Appendix A. Supplementary data

Supplementary data to this article can be found online at https://doi.org/10.1016/j.mattod.2026.103280.

Data availability

Data will be made available on request.

References

[1] Z.C. Cordero, B.E. Knight, C.A. Schuh, Six decades of the hall–petch effect – a survey of grain-size strengthening studies on pure metals, Int. Mater. Rev. 61 (8) (2016) 495–512, https://doi.org/10.1080/09506608.2016.1191808.
[2] C. Suryanarayana, et al., Grain size effects in nanocrystalline materials, J. Mater. Res. 7 (8) (1992) 2114–2118.
[3] C.A. Schuh, K. Lu, Stability of nanocrystalline metals: the role of grain-boundary chemistry and structure, MRS Bull. 46 (3) (2021) 225–235, https://doi.org/10.1557/s43577-021-00055-x.
[4] L. Zhang, C. Lu, K. Tieu, A Review on atomistic simulation of grain boundary behaviors in face-centered cubic metals, Comput. Mater. Sci 118 (2016) 180–191, https://doi.org/10.1016/j.commatsci.2016.03.021.
[5] M.A. Meyers, A. Mishra, D.J. Benson, Mechanical properties of nanocrystalline materials, Prog. Mater Sci. 51 (4) (2006) 427–556, https://doi.org/10.1016/j.pmatsci.2005.08.003.
[6] E.P. George, W.A. Curtin, C.C. Tasan, High entropy alloys: a focused review of mechanical properties and deformation mechanisms, Acta Mater. 188 (2020) 435–474.
[7] Y. Ma, et al., High-entropy energy materials: challenges and new opportunities, Energy Environ. Sci. 14 (5) (2021) 2883–2905, https://doi.org/10.1039/D1EE00505G.
[8] N. Zhou, et al., Stabilization of nanocrystalline alloys at high temperatures via utilizing high-entropy grain boundary complexions, Scr. Mater. 124 (2016) 160–163, https://doi.org/10.1016/j.scriptamat.2016.07.014.
[9] E.P. George, D. Raabe, R.O. Ritchie, High-entropy alloys, Nat. Rev. Mater. 4 (8) (2019) 515–534, https://doi.org/10.1038/s41578-019-0121-4.
[10] Y.F. Ye, et al., High-entropy alloy: challenges and prospects, Mater. Today 19 (6) (2016) 349–362, https://doi.org/10.1016/j.mattod.2015.11.026.
[11] B. Cantor, Multicomponent high-entropy cantor alloys, Prog. Mater Sci. 120 (2021) 100754.
[12] J.-W. Yeh, Alloy design strategies and future trends in high-entropy alloys, JOM 65 (12) (2013) 1759–1771, https://doi.org/10.1007/s11837-013-0761-6.
[13] Y. Zhang, et al., Microstructures and properties of high-entropy alloys, Prog. Mater Sci. 61 (2014) 1–93.
[14] L. Li, et al., Lattice-distortion dependent yield strength in high entropy alloys, Mater. Sci. Eng. A 784 (2020) 139323, https://doi.org/10.1016/j.msea.2020.139323.
[15] C. Varvenne, A. Luque, W.A. Curtin, Theory of strengthening in Fcc high entropy alloys, Acta Mater. 118 (2016) 164–176, https://doi.org/10.1016/j.actamat.2016.07.040.
[16] J. Chen, et al., A review on fundamental of high entropy alloys with promising high–temperature properties, J. Alloys Compd. 760 (2018) 15–30, https://doi.org/10.1016/j.jallcom.2018.05.067.
[17] M. Laurent-Brocq, et al., Combining tensile tests and nanoindentation to explore the strengthening of high and medium entropy alloys, Materialia 7 (2019) 100404, https://doi.org/10.1016/j.mtla.2019.100404.
[18] V. Maier-Kiener, et al., Nanoindentation testing as a powerful screening tool for assessing phase stability of nanocrystalline high-entropy alloys, Mater. Des. 115 (2017) 479–485, https://doi.org/10.1016/j.matdes.2016.11.055.
[19] R. Sriharitha, B.S. Murty, R.S. Kottada, Alloying, thermal stability and strengthening in spark plasma sintered AlxCoCrCuFeNi high entropy alloys, J. Alloys Compd. 583 (2014) 419–426, https://doi.org/10.1016/j.jallcom.2013.08.176.
[20] H. Kotan, R.C. Koç, A.B. Batıbay, Remarkable thermal stability of nanocrystalline CoCrFeNi high entropy alloy achieved through the incorporation of rare-earth element samarium, Intermetallics 178 (2025) 108608, https://doi.org/10.1016/j.intermet.2024.108608.
[21] B. Cantor, et al., Microstructural development in equiatomic multicomponent alloys, Mater. Sci. Eng. A 375–377 (2004) 213–218, https://doi.org/10.1016/j.msea.2003.10.257.
[22] Y. Addab, et al., Microstructure evolution and thermal stability of equiatomic CoCrFeNi films on (0001) α-Al2O3, Acta Mater. 200 (2020) 908–921, https://doi.org/10.1016/j.actamat.2020.09.064.
[23] N.I. Muhammad Nadzri, et al., High-entropy alloy for thin film application: a review, Coatings 12 (12) (2022) 1842, https://doi.org/10.3390/coatings12121842.
[24] M.-H. Tsai, J.-W. Yeh, J.-Y. Gan, Diffusion barrier properties of AlMoNbSiTaTiVZr high-entropy alloy layer between copper and silicon, Thin Solid Films 516 (16) (2008) 5527–5530, https://doi.org/10.1016/j.tsf.2007.07.109.
[25] Y. Zou, et al., Nanocrystalline high-entropy alloys: a new paradigm in high-temperature strength and stability, Nano Lett. 17 (3) (2017) 1569–1574, https://doi.org/10.1021/acs.nanolett.6b04716.
[26] G. Wu, et al., Symbiotic crystal-glass alloys via dynamic chemical partitioning, Mater. Today 51 (2021) 6–14, https://doi.org/10.1016/j.mattod.2021.10.025.
[27] Y. Xiao, et al., Micro-compression studies of face-centered cubic and body-centered cubic high-entropy alloys: size-dependent strength, strain rate sensitivity, and activation volumes, Mater. Sci. Eng. A 790 (2020) 139429, https://doi.org/10.1016/j.msea.2020.139429.
[28] D. Depla, W.P. Leroy, Magnetron sputter deposition as visualized by Monte Carlo modeling, Thin Solid Films 520 (20) (2012) 6337–6354.
[29] V. Soare, et al., Electrochemical deposition and microstructural characterization of AlCrFeMnNi and AlCrCuFeMnNi high entropy alloy thin films, Appl. Surf. Sci. 358 (2015) 533–539, https://doi.org/10.1016/j.apsusc.2015.07.142.
[30] P.R. Willmott, J.R. Huber, Pulsed laser vaporization and deposition, Rev. Mod. Phys. 72 (1) (2000) 315–328, https://doi.org/10.1103/RevModPhys.72.315.
[31] K. Sturm, S. Fähler, H.-U. Krebs, Pulsed laser deposition of metals in low pressure inert gas, Appl. Surf. Sci. 154 (2000) 462–466.
[32] M. Ghidelli, et al., Engineering plasmonic nanostructured surfaces by pulsed laser deposition, Appl. Surf. Sci. 434 (2018) 1064–1073, https://doi.org/10.1016/j.apsusc.2017.11.025.
[33] P. Gondoni, et al., Fabrication of nano-engineered transparent conducting oxides by pulsed laser deposition, J. Vis. Exp. 72 (2013) 50297, https://doi.org/10.3791/50297.
[34] M. Ghidelli, et al., Novel class of nanostructured metallic glass films with superior and tunable mechanical properties, Acta Mater. 213 (2021) 116955.
[35] F. Bignoli, et al., Novel class of crystal/glass ultrafine nanolaminates with large and tunable mechanical properties, ACS Appl. Mater. Interfaces 16 (27) (2024) 35686–35696.
[36] M.D. Cropper, Thin films of AlCrFeCoNiCu high-entropy alloy by pulsed laser deposition, Appl. Surf. Sci. 455 (2018) 153–159, https://doi.org/10.1016/j.apsusc.2018.05.172.

[37] E.A. Laszlo, et al., Characteristics of thin high entropy alloy films grown by pulsed laser deposition, Coatings 12 (8) (2022) 1211, https://doi.org/10.3390/coatings12081211.
[38] B.R. Braeckman, et al., Impurity-controlled film growth and elastic properties of CoCrCuFeNi thin films, Surf. Coat. Technol. 315 (2017) 475–483, https://doi.org/10.1016/j.surfcoat.2017.03.014.
[39] S. Nam, et al., Deformation behavior of nanocrystalline and ultrafine-grained CoCrCuFeNi high-entropy alloys, J. Mater. Res. 34 (5) (2019) 720–731, https://doi.org/10.1557/jmr.2018.477.
[40] E. Besozzi, et al., Amorphous, ultra-nano- and nano-crystalline tungsten-based coatings grown by pulsed laser deposition: mechanical characterization by surface brillouin spectroscopy, Mater. Des. 106 (2016) 14–21, https://doi.org/10.1016/j.matdes.2016.04.096.
[41] S. Mahieu, et al., Biaxial alignment in sputter deposited thin films, Thin Solid Films 515 (4) (2006) 1229–1249, https://doi.org/10.1016/j.tsf.2006.06.027.
[42] M. Sivakumar, A. Dasgupta, Selected area electron diffraction, a technique for determination of crystallographic texture in nanocrystalline powder particle of Alloy 617 ODS and comparison with precession electron diffraction, Mater Charact 157 (2019) 109883, https://doi.org/10.1016/j.matchar.2019.109883.
[43] J.R. Sambles, The resistivity of thin metal films—some critical remarks, Thin Solid Films 106 (4) (1983) 321–331, https://doi.org/10.1016/0040-6090(83)90344-9.
[44] P.X. Yan, et al., Metastable phase separation and crystalline orientation feature of electromagnetic levitation processed CoCrCuFeNi high entropy alloy, Acta Mater. 269 (2024) 119778, https://doi.org/10.1016/j.actamat.2024.119778.
[45] L.J. Zhang, et al., Microstructure and mechanical behaviors of GdxCoCrCuFeNi high-entropy alloys, Mater. Sci. Eng. A 707 (2017) 708–716, https://doi.org/10.1016/j.msea.2017.09.102.
[46] J. Liu, Molecular dynamic study of temperature dependence of mechanical properties and plastic inception of CoCrCuFeNi high-entropy alloy, Phys. Lett. A 384 (22) (2020) 126516, https://doi.org/10.1016/j.physleta.2020.126516.
[47] F. Tian, et al., *Ab initio* investigation of high-entropy alloys of 3 d elements, Phys. Rev. B 87 (7) (2013) 075144, https://doi.org/10.1103/PhysRevB.87.075144.
[48] H.S. Kim, M.B. Bush, The effects of grain size and porosity on the elastic modulus of nanocrystalline materials, Nanostructured Mater. 11 (3) (1999) 361–367, https://doi.org/10.1016/S0965-9773(99)00052-5.
[49] L. Zhang, Y. Shibuta, Inverse Hall-Petch relationship of high-entropy alloy by atomistic simulation, Mater. Lett. 274 (2020) 128024, https://doi.org/10.1016/j.matlet.2020.128024.
[50] H. Zhang, et al., *In situ* mechanical characterization of CoCrCuFeNi high-entropy alloy micro/nano-pillars for their size-dependent mechanical behavior, Mater. Res. Express 3 (9) (2016) 094002, https://doi.org/10.1088/2053-1591/3/9/094002.
[51] S. Zak, et al., Accurate measurement of thin film mechanical properties using nanoindentation, J. Mater. Res. 37 (7) (2022) 1373–1389, https://doi.org/10.1557/s43578-022-00541-1.
[52] S. Yoshida, et al., Effect of elemental combination on friction stress and Hall-Petch relationship in face-centered cubic high / medium entropy alloys, Acta Mater. 171 (2019) 201–215, https://doi.org/10.1016/j.actamat.2019.04.017.
[53] M.M. Abdullah, F.M. Rajab, S.M. Al-Abbas, Structural and optical characterization of Cr2O3 nanostructures: evaluation of its dielectric properties, AIP Adv. 4 (2) (2014) 027121, https://doi.org/10.1063/1.4867012.
[54] M.K. Kini, et al., Nanocrystalline equiatomic CoCrFeNi alloy thin films: are they single phase Fcc? Surf. Coat. Technol. 410 (2021) 126945 https://doi.org/10.1016/j.surfcoat.2021.126945.
[55] M. Arfaoui, G. Radnóczi, V. Kovács Kis, Transformations in CrFeCoNiCu high entropy alloy thin films during in-situ annealing in TEM, Coatings 10 (1) (2020) 60, https://doi.org/10.3390/coatings10010060.
[56] Y.-P. Xie, S.-J. Zhao, The energetic and structural properties of Bcc NiCu, FeCu alloys: a first-principles study, Comput. Mater. Sci 50 (9) (2011) 2586–2591, https://doi.org/10.1016/j.commatsci.2011.03.046.
[57] K.N. Campo, et al., Melting behavior and globular microstructure formation in semi-solid CoCrCu FeNi high-entropy alloys, J. Mater. Sci. Technol. 52 (2020) 207–217, https://doi.org/10.1016/j.jmst.2020.04.009.
[58] S. Lee, et al., Structure and hardness of in situ synthesized nano-oxide strengthened CoCrFeNi high entropy alloy thin films, Scr. Mater. 203 (2021) 114044, https://doi.org/10.1016/j.scriptamat.2021.114044.
[59] Krapivka, N. A.; Firstov, S. A.; Karpets, M. V.; Myslivchenko, A. N.; Gorban', V. F. Features of Phase and Structure Formation in High-Entropy Alloys of the AlCrFeCoNiCu x System (x = 0, 0.5, 1.0, 2.0, 3.0). Phys. Met. Metallogr. 2015, *116* (5), 467–474. https://doi.org/10.1134/S0031918X15030084.
[60] A. Bailini, et al., Pulsed laser deposition of tungsten and tungsten oxide thin films with tailored structure at the nano- and mesoscale, Appl. Surf. Sci. 253 (19) (2007) 8130–8135, https://doi.org/10.1016/j.apsusc.2007.02.145.
[61] E. Besozzi, et al., Thermomechanical properties of amorphous metallic tungsten-oxygen and tungsten-oxide coatings, Mater. Des. 165 (2019) 107565, https://doi.org/10.1016/j.matdes.2018.107565.
[62] Y. Zhao, et al., Effect of grain size on the strain rate sensitivity of CoCrFeNi high-entropy alloy, Mater. Sci. Eng. A 782 (2020) 139281, https://doi.org/10.1016/j.msea.2020.139281.
[63] Li, C. Application of optoacoustic techniques and first principle calculation to thin films elasticity characterization. PhD thesis. https://theses.fr/2019PA131091.
[64] Y. Ma, et al., Nanoindentation study on the creep characteristics of high-entropy alloy films: Fcc versus Bcc structures, Int. J. Refract. Met. Hard Mater 54 (2016) 395–400, https://doi.org/10.1016/j.ijrmhm.2015.08.010.
[65] F. Siska, et al., Twinning in CoCrFeNiMn high entropy alloy induced by nanoindentation, Mater. Sci. Eng. A 784 (2020) 139297, https://doi.org/10.1016/j.msea.2020.139297.
[66] J.G. Gigax, et al., Micro- and mesoscale mechanical properties of an ultra-fine grained CrFeMnNi high entropy alloy produced by large strain machining, Scr. Mater. 178 (2020) 508–512, https://doi.org/10.1016/j.scriptamat.2019.11.042.
[67] B.R. Braeckman, et al., The nanostructure and mechanical properties of nanocomposite Nbx-CoCrCuFeNi thin films, Scr. Mater. 139 (2017) 155–158, https://doi.org/10.1016/j.scriptamat.2017.06.046.
[68] L.L. Xiao, et al., Ultra-strong nanostructured CrMnFeCoNi high entropy alloys, Mater. Des. 194 (2020) 108895, https://doi.org/10.1016/j.matdes.2020.108895.
[69] W. Liao, et al., Nanocrystalline high-entropy alloy (CoCrFeNiAl0.3) thin-film coating by magnetron sputtering, Thin Solid Films 638 (2017) 383–388, https://doi.org/10.1016/j.tsf.2017.08.006.
[70] Z. Wu, et al., Recovery, recrystallization, grain growth and phase stability of a family of FCC-structured multi-component equiatomic solid solution alloys, Intermetallics 46 (2014) 131–140, https://doi.org/10.1016/j.intermet.2013.10.024.
[71] V.Y. Gertsman, R. Birringer, On the room-temperature grain growth in nanocrystalline copper, Scr. Metall. Mater. 30 (5) (1994) 577–581, https://doi.org/10.1016/0956-716X(94)90432-4.
[72] H.R. Rezaei Ashtiani, A.A. Shayanpoor, Effect of initial grain size on the hot deformation behavior and microstructural evolution of pure copper, Acta Metall. Sin. Engl. Lett. 35 (4) (2022) 662–678, https://doi.org/10.1007/s40195-021-01346-7.
[73] X.C. Liu, H.W. Zhang, K. Lu, Strain-induced ultrahard and ultrastable nanolaminated structure in nickel, Science 342 (6156) (2013) 337–340, https://doi.org/10.1126/science.1242578.
[74] A.J. Detor, C.A. Schuh, Microstructural evolution during the heat treatment of nanocrystalline alloys, J. Mater. Res. 22 (11) (2007) 3233–3248, https://doi.org/10.1557/JMR.2007.0403.
[75] T.R. Malow, C.C. Koch, Grain growth in nanocrystalline iron prepared by mechanical attrition, Acta Mater. 45 (5) (1997) 2177–2186, https://doi.org/10.1016/S1359-6454(96)00300-X.
[76] K.A. Darling, et al., Thermal stability of nanocrystalline Fe–Zr alloys, Mater. Sci. Eng. A 527 (15) (2010) 3572–3580, https://doi.org/10.1016/j.msea.2010.02.043.
[77] J. Eckert, J.C. Holzer, W.L. Johnson, Thermal stability and grain growth behavior of mechanically alloyed nanocrystalline Fe-Cu alloys, J. Appl. Phys. 73 (1) (1993) 131–141, https://doi.org/10.1063/1.353890.
[78] K.-Y. Tsai, M.-H. Tsai, J.-W. Yeh, Sluggish diffusion in Co–Cr–Fe–Mn–Ni high-entropy alloys, Acta Mater. 61 (13) (2013) 4887–4897, https://doi.org/10.1016/j.actamat.2013.04.058.
[79] F. Bignoli, et al., Extending mechanical size effect range of thin film metallic glasses by nanoengineering their atomic and nanostructure, Acta materialia 300 (2025) 121456, https://doi.org/10.1016/j.actamat.2025.121456.
[80] Z. An, et al., Solid-solution CrCoCuFeNi high-entropy alloy thin films synthesized by sputter deposition, Mater. Res. Lett. 3 (4) (2015) 203–209, https://doi.org/10.1080/21663831.2015.1048904.
[81] T.Y. Tsui, C.A. Ross, G.M. Pharr, A method for making substrate-independent hardness measurements of soft metallic films on hard substrates by nanoindentation, J. Mater. Res. 18 (6) (2003) 1383–1391, https://doi.org/10.1557/JMR.2003.0190.
[82] G. Carlotti, Elastic characterization of transparent and opaque films, multilayers and acoustic resonators by surface brillouin scattering: a review, Appl. Sci. 8 (1) (2018) 124.
[83] K. Mongkolsuttirat, J. Buajarern, Uncertainty evaluation of crystallite size measurements of nanoparticle using x-ray diffraction analysis (XRD), J. Phys. Conf. Ser. 1719 (1) (2021) 012054, https://doi.org/10.1088/1742-6596/1719/1/012054.
[84] J. Náhlík, I. Kašpárková, P. Fitl, Study of quantitative influence of sample defects on measurements of resistivity of thin films using van Der Pauw method, Measurement 44 (10) (2011) 1968–1979, https://doi.org/10.1016/j.measurement.2011.08.023.
[85] W.C. Oliver, G.M. Pharr, Measurement of hardness and elastic modulus by instrumented indentation: advances in understanding and refinements to methodology, J. Mater. Res. 19 (1) (2004) 3–20, https://doi.org/10.1557/jmr.2004.19.1.3.